Research Article Vol. 31, No. 17 / 14 Aug 2023 / Optics Express 27332
Optics EXPRESS

Highly-sensitive temperature sensor based on photopolymerized-waveguide embedded Mach-Zehnder interferometer

JIABIN WANG,[1] XINGYU YANG,[1] YANRU KOU,[1] DI TONG,[1] ANZHI WANG,[1] CHONG NIU,[1] HAORAN MENG,[2] SONG LI,[1] TAO GENG,[1,3,*] AND WEIMIN SUN[1]

[1]*Key Laboratory of In-Fiber Integrated Optics of Ministry of Education, Harbin Engineering University, Harbin 150001, China*
[2]*Changchun Institute of Optics, Fine Mechanics and Physics, Chinese Academy of Sciences, Changchun 130033, China*
[3]*State Key Laboratory of Applied Optics, Changchun Institute of Optics, Fine Mechanics and Physics, Chinese Academy of Sciences, Changchun 130033, China*
[*]*gengtao_hit_oe@126.com*

Abstract: Biology, medicine, and chemistry all rely heavily on highly sensitive optical fiber temperature sensors. To the best of our knowledge, this research introduces a unique design framework for high-performance fiber temperature sensors that helps eliminate the all-fiber interferometers' sensitivity bottleneck. A section of photopolymerized waveguide is embedded in a typical Mach-Zehnder interferomenter framework with multimode fiber-single mode fiber-multimode fiber (MSM) structure. The thermal-optical coefficient (TOC) of the photopolymerized waveguide core, which is created via the fiber-end lithography technique, differs dramatically from that of the resin cladding. Due to the considerable TOC difference, the phase difference between the interfering beams significantly increases as the temperature changes. The fundamental variables affecting temperature sensitivity are conceptually explored and experimentally verified. The suggested device achieves a typical temperature sensitivity of 1.15 nm/°C in the range of 30–100°C, which is about 10 times as high as that of the all-fiber MSM sensors. The suggested designing framework offers a fresh thought for creating high-performing fiber optic temperature sensors.

1. Introduction

The development of high-sensitivity temperature sensors is of great significance for bio-engineering [1], pharmaceutical engineering [2], nuclear reactor monitoring [3] and lithium battery detecting [4]. Optical fiber sensors provide several benefits over electronic sensors, including compact size, lightweight, high sensitivity, and excellent resistance to corrosion from chemicals and electromagnetic interference. Fiber temperature sensors based on Fiber Bragg Gratings (FBG) [5], Long-period Fiber Gratings (LPFG) [6], Fabry–Perot interferometers (FPI) [7], and Mach-Zehnder interferometers (MZI) [8,9] have been developed and applied for practical applications in recent years. Among these efforts, interferometric frameworks, particularly MZI-based sensors, stand out for their clear benefits of simplicity, affordability, and high strength.

The common approaches to construct MZIs are mode field mismatching [10], core-offset splicing [11], side polishing [12], and fiber tapering [13]. The most prevalent MZI framework is a multi-mode fiber (MMF) integrated sandwich construction. The MMF has two components that function as the beam combiner and splitter, respectively. The interference between the fundamental mode and the cladding modes forms multiple dips in the transmission spectrum. Due to the well-known thermal-optical and thermal-expansion effects, these dips are sensitive to

#493552 https://doi.org/10.1364/OE.493552
Journal © 2023 Received 19 Apr 2023; revised 9 Jul 2023; accepted 20 Jul 2023; published 1 Aug 2023

Optics EXPRESS

temperature changes. However, the extremely tiny thermal-optical coefficient (TOC) difference between the doped-silica core and pure cladding substantially limits the temperature sensitivity of these all-fiber MZI sensors. In order to break the bottleneck, functional materials with greater TOC than silica are coated on the ordinary MZI structures to alter the effective refractive index (RI) of the cladding modes [14,15]. Although the temperature sensitivity has been improved somewhat, there designing frameworks are only able to change the effective RI of the cladding modes by changing the boundary condition. The gain in sensitivity is still limited. Additionally, the coated fiber structure makes packing difficult and decreases the mechanical strength of the devices, which are always tapered or polished to be extremely thin in order to produce a strong evanescent field.

In this paper, we propose and demonstrate a novel, to the best of our knowledge, designing framework for highly sensitive temperature sensors based on photopolymerized-waveguide embedded Mach-Zehnder interferometer (PWE-MZI). The light involved in the interference passes through the core and the cladding of the photopolymerized waveguide, respectively. The photopolymerized waveguide consists of a green-light-cured polymer core and a UV-light-cured resin cladding. By injecting a 520 nm-laser into a sigle-mode fiber (SMF), we first obtain a solidified polymer core between the gap of the two SMFs through the fiber-end lithography technique. Then the commercially available UV-curing resin adhesive is dropped into the gap and cured to connect the SMF. Finally, we embed two sections of MMFs on each side of the photopolymerized waveguide to develop an MZI. The different core and cladding materials contribute to a significant TOC difference. Thus we successfully obtain a sensor with a temperature sensitivity 10 times higher than that of the conventional sandwich-structure sensors.

2. Fabrication and principle

The fabrication process of the sensor is mainly divided into three steps. Firstly, two sections of standard telecommunication single-mode fibers (G652, YOFC Co., Ltd) with a core/cladding diameter of 9/125 μm are stripped of the coatings and cleaved by FC-6S (Sumitomo Electric Industrial Co. Ltd). Both of them are mounted on a pair of 6-axis manual stages NFP-6561 (Zolix Instruments Co., Ltd.) and aligned using two-dimensional machine vision. The NFP-6561 accurately controls the separation between the two fiber end faces, as seen in Fig. 1 (a).

Secondly, the photopolymerizable solution is injected into the space between the two fibers. The solution reported here is composed of three components: pentaerythritol triacrylate, methyldiethanolamine, and eosin Y [16]. A semiconductor laser with tail fiber couples 520 nm laser to two SMFs through a 3-dB coupler as shown in Fig. 1 (b). When eosin is exposed to 520 nm light, the triplet state of eosin reacts with the amine to initiate the polymerization of the acrylate monomer. The output field of the SMF develops a solid polymer column between the SMF ends [seen in Fig. 2(a)]. The so-called fiber-end lithography technique is realized. The unreacted solution is washed off by ethanol. Parameters including laser power and exposure time affected the geometry of the polymer core [17]. In the experiment, the diameter of the polymer core is designed to be 9 μm, which is consistent with that of the SMF. After a few tentative experiments, the laser power and the exposure time are determined to be 6 mW and 1 minute, respectively. Fig. 2(b) shows the micrograph of a section of polymer core with a measured diameter of 11 μm and length of 150 μm. Then resin glue NOA 61 (Norland Products Inc.) is also dropped into the gap and cured by UV lamp as shown in Fig. 1 (c). In addition to serving as cladding, the NOA 61 also securely links the SMFs. As a result, a photopolymerized waveguide is formed and embedded in the SMF as shown in Fig. 2(c).

Finally, we used a homemade precision fiber cleaving system to cut off the photopolymerized-waveguide embedded SMF with a certain length L_1 away from the photopolymerized waveguide layer. The process is monitored by a microscopic imaging system. Then, a segment of MMF with a core/cladding diameter of 60/125 μm (SI 60/125-12/250, YOFC Co., Ltd) is inserted in the SMF.

Optics EXPRESS

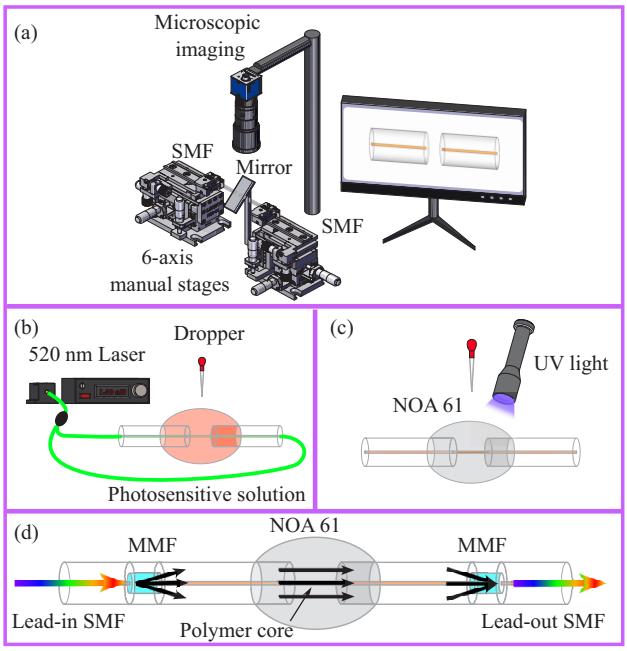

Fig. 1. Schematic diagram of the preparation process.

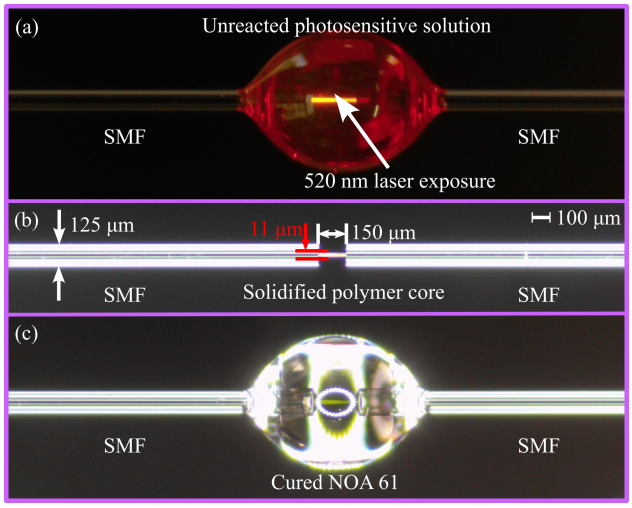

Fig. 2. The micrograph of the PWE-MZI during the fabrication. (a) Photopolymerizable solution curing. (b) Solidified polymer core. (c) NOA 61 curing.

Similarly, another segment of MMF is also embedded in another side of the photopolymerized waveguide layer with the same distance. The total length of the SMF between the two MMFs is labeled L_{smf}, where $L_{smf} = 2L_1$. We finally obtained the PWE-MZI.

The schematic diagram of the PWE-MZI is shown in Fig. 1 (d). The lead-in SMF injects the broadband light, which is then transmitted as the fundamental mode. A part of the light enters the cladding of the followed SMF after passing through the first MMF and propagates ahead as cladding modes. The remainder continues to propagate along the fiber core. When

Optics EXPRESS

the light reaches the photopolymerized waveguide, the cladding modes pass through the NOA 61 layer while the fundamental mode passes through the polymer core. The cladding modes and the fundamental mode are finally combined in the second MMF and interference occurs. The interference signal propagates along the lead-out SMF and is recorded by the spectrograph. In the experiment, we use a typical 300 μm-long MMF as the beam splitter and combiner. The total length of SMF between the MMF (L_{smf}) is determined to 1200 μm to produce a satisfactory transmission spectrum. It is worth noting that because the RI of the three-component photosensitive polymer (1.52) is lower than NOA 61 (1.56), a part of the light leaks to the cladding from the core. Investigation of the light energy distribution in the PWE-MZI is conducted using simulation based on the beam propagation method (BPM). All the fiber parameters are consistent with those provided by the manufacturer. The length of the photopolymerized waveguide (L_{pw}) is set to 200 μm. At point "a" [seen in Fig. 3], the light energy in the fiber core leaks to the cladding due to the mode mismatch. At point "c", the lower RI of the core than the cladding of the photopolymerized waveguide also makes a part of light escaping from the core. The mode field in the cross-section at points "c" and "d" indicates that the photopolymerized waveguide only slightly disturbs the energy distribution of the original cladding modes, but does not lead to mode reconstruction. Although other commercially available UV-cured adhesives exhibit a lower refractive index (lower than 1.52), NOA 61 is more widely used in bonding quartz materials and is recognized for its bond reliability.

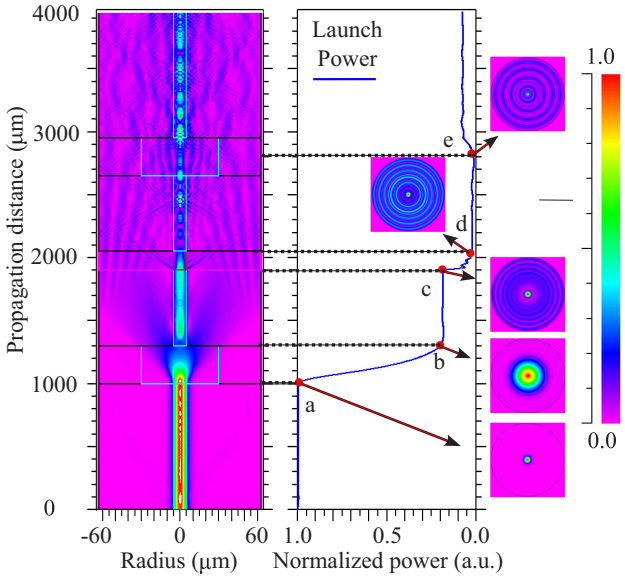

Fig. 3. Simulation results of the light energy distribution in the PWE-MZI.

Considering a simplified case of two beam interference, the interference intensity (I) is expressed as [18]

$$I = I_1 + I_2 + 2\sqrt{I_1 I_2}\cos(\Delta\phi) \tag{1}$$

where I_1 and I_2 are the intensity of the cladding modes and the fundamental mode, respectively. $\Delta\phi$ represents the phase difference between the two modes in which the interference occurs. For the PWE-MZI, $\Delta\phi$ is expressed as [19]

$$\Delta\phi = \frac{2\pi}{\lambda}\left(\Delta n_{\text{eff}}^{\text{smf}} L_{\text{smf}} + \Delta n_{\text{eff}}^{\text{pw}} L_{\text{pw}}\right) \tag{2}$$

Optics EXPRESS

where λ is the wavelength. $\Delta n_{\text{eff}}^{\text{smf}}$ and $\Delta n_{\text{eff}}^{\text{pw}}$ represent the effective RI difference of the core mode and cladding modes in the SMF and photopolymerized waveguide, respectively. L_{smf} and L_{pw} refer to the total length of the SMF between the two MMFs and the photopolymerized waveguide, respectively. When the condition $\Delta\phi = (2m+1)\pi (m = 1, 2, 3\cdots)$ is satisfied, destructive interference occurs. The wavelength of the m^{th}-order attenuation dip is determined by [19]

$$\lambda_m = \frac{2}{(2m+1)}\left(\Delta n_{\text{eff}}^{\text{smf}} L_{\text{smf}} + \Delta n_{\text{eff}}^{\text{pw}} L_{\text{pw}}\right) \tag{3}$$

The free spectral range (FSR) of the PWE-MZI is deduced and approximated using Taylor expanding [20]

$$FSR = \frac{\lambda^2}{\left(\Delta n_{\text{eff}}^{\text{smf}} L_{\text{smf}} + \Delta n_{\text{eff}}^{\text{pw}} L_{\text{pw}}\right)} \tag{4}$$

According to Eq. (4), the FSR is inversely proportional to the optical path difference of the coherent light when a certain wavelength λ is given.

The temperature sensitivity of the PWE-MZI is derived by taking the partial derivative of Eq. (3)

$$\frac{\partial \lambda}{\partial T} \propto \left(\frac{\partial \Delta n_{\text{eff}}^{\text{smf}}}{\partial T} L_{\text{smf}} + \Delta n_{\text{eff}}^{\text{smf}} \frac{\partial L_{\text{smf}}}{\partial T}\right) + \left(\frac{\partial \Delta n_{\text{eff}}^{\text{pw}}}{\partial T} L_{\text{pw}} + \Delta n_{\text{eff}}^{\text{pw}} \frac{\partial L_{\text{pw}}}{\partial T}\right) \tag{5}$$

where $\partial \Delta n_{\text{eff}} / \partial T$ and $\partial L_{\text{pw}} / \partial T$ represent the TOC and TEC difference between the core and the cladding of the waveguide. Due to the difference between the core and cladding material of the photopolymerized waveguide, we obtain a large $\partial \Delta n_{\text{eff}}^{\text{pw}} / \partial T$ and thus a high-temperature sensitivity. Since NOA 61 has adhered to the polymer core, the thermal expansion of the two can be ignored here.

3. Experimental results and discussions

3.1. Investigation on the repeatability of the PWE-MZI

The repeatability of PWE-MZI is a crucial index when assessing the device's applicability. In this work, we experimentally evaluate the repeatable fabrication capability of the device in detail. Four PWE-MZIs all having the same parameters (L_{mmf}=300 μm, L_{pw}=150 μm, L_{smf}=1200 μm) have been fabricated and tested. The comparison of their transmission spectra is shown in Fig. 4.

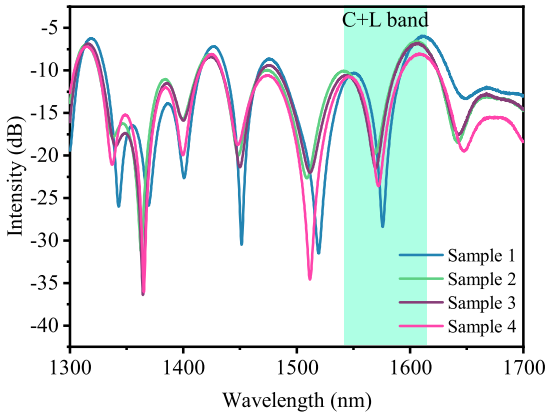

Fig. 4. The transmission spectra of the five PWE-MZI all having the same parameters.

Optics EXPRESS

According to Eqs. (1) and (3), L_{smf}, L_{pw} and the RI difference between the interference modes (Δn_{eff}) are main parameters that directly affect the transmission spectrum. In addition, cladding modes excited by different L_{mmf} also determine Δn_{eff} and thus affect the position of characteristic dips in the transmission spectrum. The extinction ratio is mathematically expressed as

$$K = 2\frac{\sqrt{I_1 I_2}}{(I_1 + I_2)} \tag{6}$$

According to Eq. (6), the extinction ratio of the interference signal is determined by the intensity of the modes involved in the interference. When $I_1 = I_2$ is satisfied, K reaches its highest value. The diameter and uniformity of the polymer core have an impact on the extinction ratio K and the energy of the modes for the proposed PWE-MZI. Herein, we use a microscopic imaging system to help determine the length of each waveguide element. Meanwhile, the core diameter of the photopolymerized waveguide determined by the power and exposure time of the 520-nm laser are held constant. As shown in Fig. 4, the maximum wavelength and extinction ratio fluctuations of the target dip in C+L band marked in light green are 6.4 nm and 8.62 dB, respectively, which indicates satisfactory spectral repeatability.

3.2. *Influence of L_{pw} on temperature sensitivity*

According to Eqs. (3) and (5), the controllable length of the photopolymerized waveguide (L_{pw}) not only affects the transmission spectrum but also contributes to the temperature sensitivities. We fabricate PWE-MZI with various L_{pw} and characterize each of their temperature responses. The spectra evolution with L_{pw} is depicted in Fig. 5.

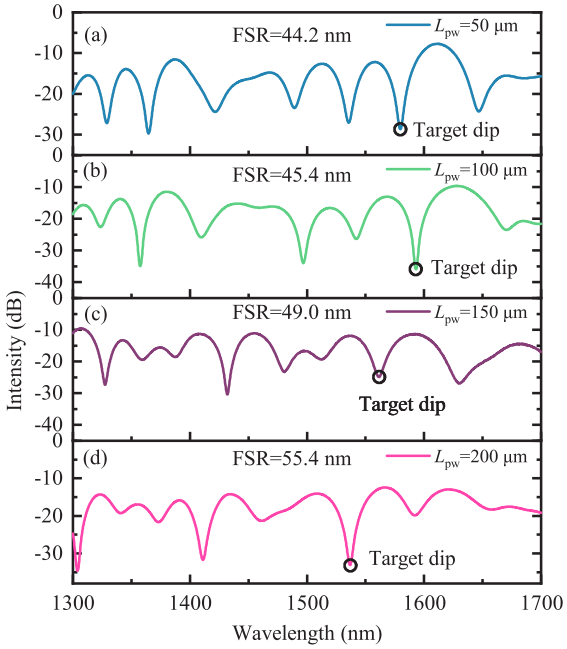

Fig. 5. The spectra evolution with L_{pw}. (a) L_{pw}=50 μm; (b) L_{pw}=100 μm; (c) L_{pw}=150 μm; (d) L_{pw}=200 μm.

The curing of the photopolymerized solution occurs due to the "self-trapping effect" [21]. This is so that only the solution exposed to a 520 nm laser higher than the curing threshold will be solidified. And the green laser travels forward along the solidified polymer with a higher RI than

Optics EXPRESS

the uncured solution. The energy field coming out of the SMF is able to be fitted by a Gaussian function. The energy density decays from the center to the edge. When photopolymerization starts, the incident photon energy is used for several chemical reactions, including the formation of peroxides. In the case of a short exposure time, only the brightest region of the guided Gaussian-type beam reaches the polymerization threshold [22]. Although there are high-order modes in the standard communication SMF for 520 nm light, we still obtain an approximate Gaussian-like emission field by means of mechanical scrambling [23]. As a result, we are able to fabricate a uniform cylindrical-photopolymerized core by setting the laser energy reasonably. However, this also limits the length of the photopolymerized waveguide. For longer polymer cores, more exposure time is required to ensure adequate polymerization.

In the experiment, we fabricated samples with L_{pw} in the range of 50-200 μm while the length of the SMF is fixed to 1200 μm. The FSRs of the four transmission spectra around 1550 nm are 44.2 nm, 45.4 nm, 49.0 nm, and 55.4 nm, respectively. It is obvious that the FSR increases with the L_{pw}, which is consistent with Eq. (4). Fast-Fourier transform (FFT) is applied to investigate the number and the energy distribution of interfering modes.

Two dominant peaks in the spatial frequency spectra represent the main cladding modes with which the interference occurs. With the increase of L_{pw}, the frequency of the peaks shifts slightly to the lower frequency. Fig. 6 indicates that the FSR decreases with the increased L_{pw}. We then characterize the temperature responses of the four samples respectively. Considering the compatibility with instruments in communication bands dips near 1550 nm in the transmission spectrum are selected as the monitoring target for temperature sensing. The experimental setup is shown in Fig. 7. A thermostatic furnace with a custom V-groove on the heating plate is applied to heat the sensor. The PWE-MZI is mounted on a pair of fiber clamps and embedded in the V-groove. A quartz plate covers the sensor to ensure that the temperature measured by the sensor is consistent with the set. A thermocouple thermometer is applied to verify the temperature. Broadband light in the range of 1300 nm-1700 nm provided by a supercontinuum light source (SCL) SC-5 (YSL Photonics) is injected into the sensor. The transmission spectra are recorded by the optical spectrum analyzer (OSA) AQ6370D (YOKOGAWA Co., Ltd.) with a resolution of 0.02 nm. The temperature is set to 30 °C and increased with a step of 5 °C. Then the temperature is decreased to 30 °C. We record the evolution of the transmission spectra during heating and cooling. The relationship between the central wavelength of the dip and the applied temperature is fitted by a linear function. The results of the four samples are shown in Fig. 8.

In the heating process, the temperature sensitivities of the four samples are 0.34 nm/°C, 0.85 nm/°C, 1.15 nm/°C, and 1.21 nm/°C, respectively. In the cooling process, the sensitivities are 0.42 nm/°C, 0.85 nm/°C, 1.22 nm/°C, and 1.57 nm/°C, respectively. All the goodness of fitting (R^2) is 0.99. According to Eq. (5), the temperature sensitivity $\partial\lambda/\partial T$ is proportional to L_{pw}. Although Eq. (5) shows that $\partial\lambda/\partial T$ is also proportional to L_{smf}, the TOC of the silica fiber is so small that the effect of L_{smf} on temperature sensitivity is able to be ignored. Experimental results illustrate that the temperature sensitivity of the PWE-MZI increases with the increase of L_{pw}, which is consistent with Eq. (5). It is worth noting that when L_{pw} is 50μm and 200 μm, there is an obvious difference in sensitivity during the heating and cooling process. The reason for this difference can be attributed to the difference in TEC and thermal conductivity between the polymer core and resin cladding. The polymer waveguide with a length in the range of 100 μm to 150 μm has a better thermal response.

3.3. Influence of L_{mmf} on temperature sensitivity

Previous works have indicated that different cladding modes excited by the MMF also influence the temperature sensitivities based on MZI [24,25]. Thus we also experimentally investigate the influence of L_{mmf} on temperature sensitivity. Samples with L_{mmf} of 200 μm, 300 μm, 400 μm, and 500 μm have been fabricated. Herein the total length of the SMF between the two MMF is

Optics EXPRESS

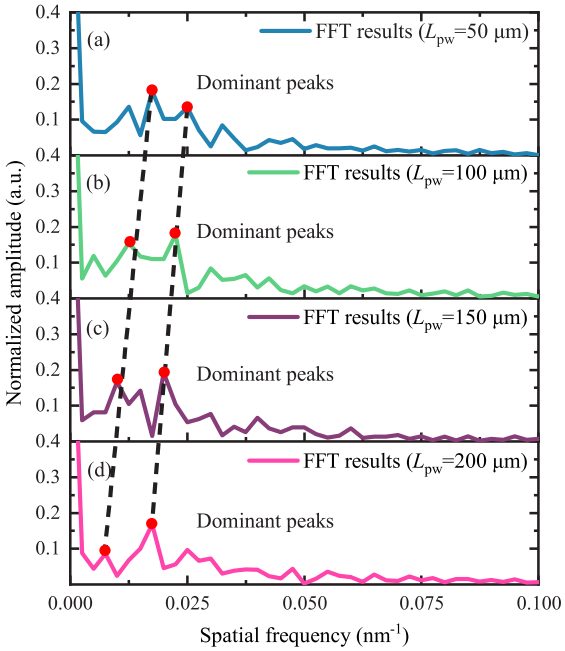

Fig. 6. Spatial frequency spectra of the PWE-MZI with different L_{pw}. (a) L_{pw}=50 μm; (b) L_{pw}=100 μm; (c) L_{pw}=150 μm; (d) L_{pw}=200 μm.

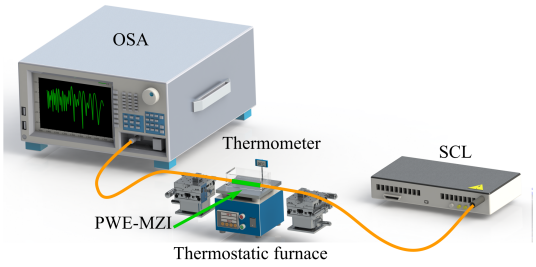

Fig. 7. Experimental setup for temperature measurement.

kept to be 1200 μm. The FFT method is performed on the spectra of PWE-MZI with different L_{mmf}. The spectrum evolution and FFT results are shown in Figs. 9 and 10, respectively.

Theoretically, the relationship between the spatial frequency and the differential modal group index as well as the interferometer length is given as [26]

$$\xi = \frac{1}{\lambda_0^2}\Delta m_{eff} L_0 \tag{7}$$

where L_0 is the total length of the interference arm, λ_0 is center wavelength, ξ is the spatial frequency and Δm_{eff} is the differential modal group index. According to Eq. (7), ξ is proportional to both L_0 and Δm_{eff}. For the PWE-MZI, $L_0 = L_{smf} + L_{pw}$. It is worth noting that we have not discussed the influence of L_{smf} on the temperature, because compared with photopolymerized waveguide with high TOC difference, the effect of L_{smf} on temperature sensitivity is negligible. When a certain L_0 is given, a smaller ξ corresponds to a smaller Δm_{eff} which means a lower-order cladding mode. For the PWE-MZI, the cladding modes transmitting in the first section of SMF

Optics EXPRESS

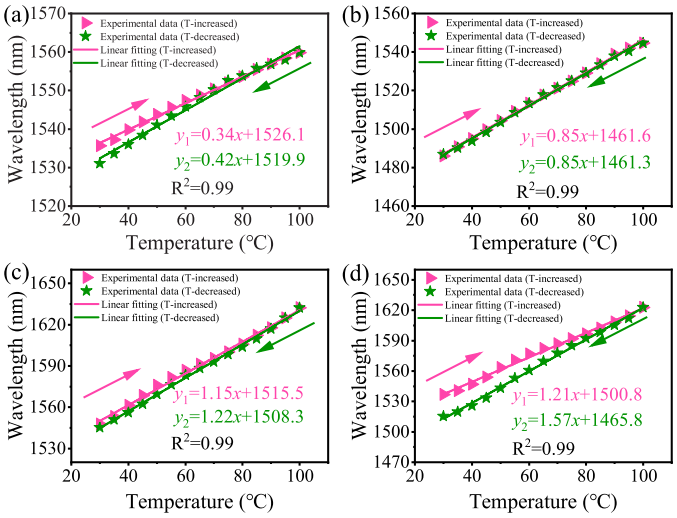

Fig. 8. Temperature sensitivities of the PWE-MZI with different L_{pw}. (a) L_{pw}=50 μm; (b) L_{pw}=100 μm; (c) L_{pw}=150 μm; (d) L_{pw}=200 μm.

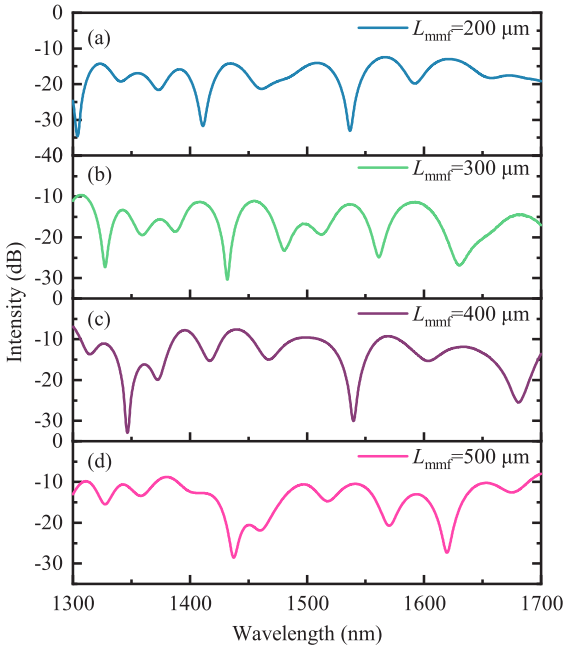

Fig. 9. The spectra evolution with L_{mmf}. (a) L_{mmf}=200 μm; (b) L_{mmf}=300 μm; (c) L_{mmf}=400 μm; (d) L_{mmf}=500 μm.

will be slightly disturbed by the short photopolymerized waveguide. Strictly speaking, Eq. (7) can only be used to qualitatively evaluate the relationship between the spatial frequency and the differential modal group index.

Fig. 10 shows that the dominant peaks in the spatial frequency spectrum shift to the lower frequency. It indicates the differential modal group index Δm_{eff} decreased with increased L_{mmf}. We are able to say that the interference occurs between the fundamental mode and lower order

Optics EXPRESS

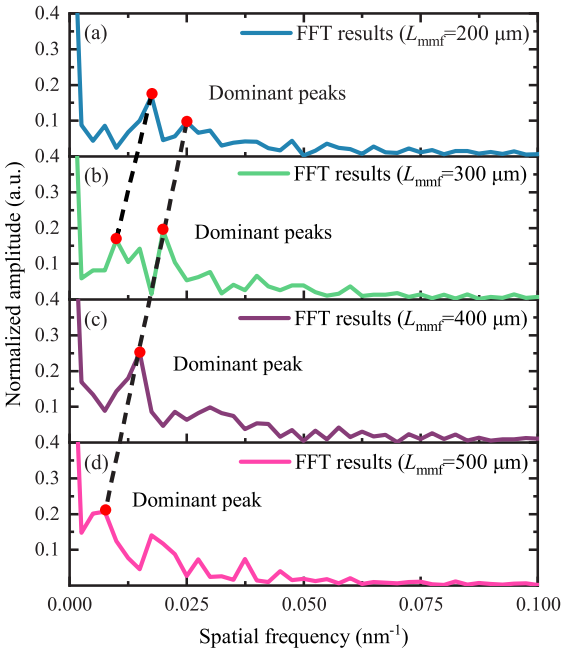

Fig. 10. Spatial frequency spectra of the PWE-MZI with different L_{mmf}. (a) L_{mmf}=200 μm; (b) L_{mmf}=300 μm; (c) L_{mmf}=400 μm; (d) L_{mmf}=500 μm.

cladding modes in the PWE-MZI with longer MMF. Such a result is consistent with the theoretical calculations in [25].

We characterize the temperature responses of those PWE-MZI with different L_{mmf} in both heating and cooling processes. The results are shown in Fig. 11.

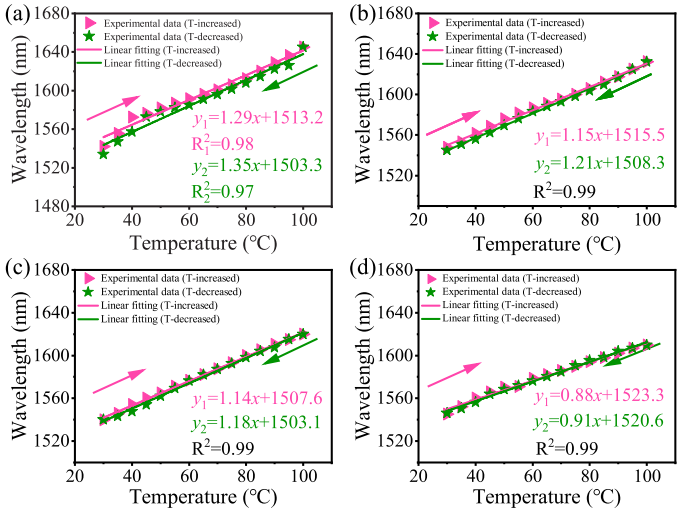

Fig. 11. Temperature sensitivities of the PWE-MZI with different L_{mmf}. (a) L_{mmf}=200 μm; (b) L_{mmf}=300 μm; (c) L_{mmf}=400 μm; (d) L_{mmf}=500 μm.

Optics EXPRESS

PWE-MZI with L_{mmf} of 200 μm exhibits a maximum sensitivity of 1.29 nm/°C and 1.35 nm/°C in the heating and cooling process, respectively. When L_{mmf} is increased to 500 μm, the sensitivity decreased to 0.88 nm/°C and 0.91 nm/°C. The temperature sensitivity degrades with the increased L_{mmf}. Although higher-order cladding modes excited by short MMFs contribute to the improvement in temperature sensitivity, the gain obtained by changing L_{mmf} is limited compared to lengthen the photopolymerized waveguide.

3.4. Discussion

MSM structure-based fiber sensors have been widely studied and applied for multiple parameters measurement due to their advantages of easy preparation, stable mechanical strength, and flexible structure. However, it is challenging to accomplish high-sensitivity temperature measurements with conventional MSM-based fiber sensors. Although functional materials such as polydimethylsiloxane (PDMS) and graphene have been coated on well-designed MSM structures to improve temperature sensitivities, the increase in sensitivity is also limited. Table 1 shows the comparison between the temperature sensing characteristics of the proposed PWE-MZI sensor and other sensors reported recently.

Table 1. A comparison between the temperature sensing performances of the proposed PWE-MZI sensor and other sensors reported recently.

References	Structure	Temperature sensitivity (nm/°C)	Dynamic range (°C)	Preparation technique
[27]	All-fiber MSM	0.13325	20-100	Alternate fiber splicing
[28]	All-fiber MSM	0.0815	25-60	Alternate fiber splicing
[29]	None-core fiber embedded MSM	0.0092	30-95	Alternate fiber splicing
[30]	Vernier effect assisted MZI	-0.27999	25-100	Alternate fiber splicing
[14]	PDMS coated MZI	0.13	50-80	Alternate fiber splicing and PDMS coating
[9]	PDMS injected interferometer	0.5&0.88	16-80	Alternate fiber splicing and side polishing
[31]	Side-polished NCF embedded MMI covered by PDMS	0.4409	30-85	Alternate fiber splicing, side polishing, and PDMS coating
[32]	PDMS coated LPFG	0.2554	20-80	UV-laser inscribing and PDMS coating
Present work	**PWE-MZI**	**Typical:1.15**	**30-100**	**fiber-end lithography technique**

The sensitivities of the all-fiber type fiber sensors described in [27–29] are significantly constrained by the low TOC of the silica fiber.Although the Vernier effect has been developed in [30] to improve the sensitivity, the maximum sensitivity is still not high enough. PDMS with high TOC has been deployed to cover the traditional silica fiber sensors. The interaction between the strong evanescent field excited by the well-designed structure and the signal light greatly enhances the sensing performances. However, these designing frameworks aim to decorate the silica fiber structure with high TOC materials. These devices could not address the issue of the low TOC of the silica optical waveguide. As a result, there is an upper limit to how much sensitivity is able to be improved. The designing framework of the PWE-MZI provides a new idea to enhance the temperature sensitivity of the MSM-structure-based sensors. We achieved a credible sensitivity of up to 1.15 nm/°C in the range of 30-100 °C due to the high TOC difference between the resin and the three-component photosensitive polymer.

Optics EXPRESS

4. Conclusion

To the best of our knowledge, this research presents a novel designing framework for the highly-sensitive temperature sensor. We remove the barrier caused by the tiny TOC difference between the core and cladding of the silica fiber by incorporating a section of a photopolymerized waveguide in the conventional MSM structure. The cladding of the photopolymerized waveguide is simply created by dropping and curing the readily available resin glue, while the polymer core of the waveguide is created using the fiber-end lithography approach. The spectral evolution and temperature sensitivities of the devices with different parameters are analyzed and characterized in detail. The experimental results show that shorter MMF and longer photopolymerized waveguides are conducive to better sensing performances. The proposed photopolymerized-waveguide embedded Mach-Zehnder interferometer (PWE-MZI) achieves a reliable temperature sensitivity of 1.15 nm/°C in the range of 30-100 °C. The advantages of easy preparation, compact structure, strong mechanical strength, and high sensitivity make the PWE-MZI competitive in the field of high-sensitivity temperature sensing.

Funding. Joint Research Fund in Astronomy under cooperative agreement between the National Natural Science Foundation of China (NSFC) and Chinese Academy of Sciences (CAS) (U2031130, U2031132); The State Key Laboratory of applied optics (SKLA02022001A02); The Fundamental Research Funds for the Central Universities to the Harbin Engineering University (3072022QBZ2501).

Disclosures. The authors declare no conflicts of interest.

Data availability. Data underlying the results presented in this paper are not publicly available at this time but may be obtained from the authors upon reasonable request.

References

1. S. Gupta, "Selective and rapid detection of soil fungi using surface modified long period fiber gratings," Optik **159**, 301–304 (2018).
2. M. R. Islam, M. M. I. Khan, S. Siraz, F. Mehjabin, M. Rahman, M. Islam, M. S. Anzum, J. A. Chowdhury, and F. Noor, "Design and analysis of a qc-spr-pcf sensor for multipurpose sensing with supremely high fom," Appl. Nanosci. **12**(1), 29–45 (2022).
3. A. K. Sang, M. E. Froggatt, D. K. Gifford, S. T. Kreger, and B. D. Dickerson, "One centimeter spatial resolution temperature measurements in a nuclear reactor using rayleigh scatter in optical fiber," IEEE Sens. J. **8**(7), 1375–1380 (2008).
4. J. Q. Huang, L. A. Blanquer, J. Bonefacino, E. R. Logan, D. A. Dalla Corte, C. Delacourt, B. M. Gallant, S. T. Boles, J. R. Dahn, H. Y. Tam, and J. M. Tarascon, "Operando decoding of chemical and thermal events in commercial na(li)-ion cells via optical sensors," Nat. Energy **5**(9), 674–683 (2020).
5. B. Du, J. He, B. J. Xu, X. Z. Xu, C. L. Fu, P. F. Li, X. Z. Xiao, S. Liu, Y. T. Yang, and Y. P. Wang, "High-density weak in-fiber micro-cavity array for distributed high-temperature sensing with millimeter spatial resolution," J. Lightwave Technol. **40**(22), 7447–7455 (2022).
6. Y. X. Zhang, X. X. Wang, X. Y. Tang, Z. H. Liu, Y. Zhang, C. Y. Sha, M. Zhang, W. Jin, J. Z. Zhang, and L. B. Yuan, "Photosensitive polymer-based micro-nano long-period fiber grating for refractive index sensing," J. Lightwave Technol. **39**(21), 6952–6957 (2021).
7. L. Y. Hou, C. L. Zhao, B. Xu, B. N. Mao, C. Y. Shen, and D. N. Wang, "Highly sensitive pdms-filled fabry-perot interferometer temperature sensor based on the vernier effect," Appl. Opt. **58**(18), 4858–4865 (2019).
8. Z. F. Wang, H. Bartelt, Z. W. Ma, Z. Y. Chen, F. F. Pang, and T. Y. Wang, "Temperature sensing characteristics of a four-core sapphire derived fiber based on supermode interference," IEEE Sens. J. **22**(20), 19366–19377 (2022).
9. H. C. Deng, X. W. Jiang, X. X. Huang, M. Chen, H. Y. Yang, Y. Cheng, C. A. X. Teng, R. H. Xu, and L. B. Yuan, "A temperature sensor based on composite optical waveguide," J. Lightwave Technol. **40**(8), 2663–2669 (2022).
10. K. Wang, X. C. Dong, M. H. Kohler, P. Kienle, Q. Bian, M. Jakobi, and A. W. Koch, "Advances in optical fiber sensors based on multimode interference (mmi): A review," IEEE Sens. J. **21**(1), 132–142 (2021).
11. H. W. Niu, S. Zhang, W. H. Chen, Y. Liu, X. Li, Y. X. Yan, S. J. Wang, T. Geng, W. M. Sun, and L. B. Yuan, "Optical fiber sensors based on core-offset structure: A review," IEEE Sens. J. **21**(20), 22388–22401 (2021).
12. M. S. Yang, Y. L. Zhu, and R. An, "Temperature and pressure sensor based on polished fiber-optic microcavity," IEEE Photonics Technol. Lett. **34**(11), 607–610 (2022).
13. X. J. Zhu, Y. Q. Pan, A. Sun, D. Sun, W. Liu, J. Cao, G. Zhang, Z. H. Han, L. Zou, Z. P. Liang, and Y. C. Shi, "High sensitivity curvature sensor based on a double-sphere tapered no-core fiber mach-zehnder interferometer," Opt. Laser Technol. **155**, 108364 (2022).
14. H. L. Su, Y. X. Wang, C. S. Guan, S. Yu, X. Y. Yu, and W. L. Yang, "Pdms-sensitized mzi fiber optic temperature sensor based on tcf-ncf-tcf structure," Opt. Fiber Technol. **73**, 103075 (2022).

Optics EXPRESS

15. D. Yi, F. Liu, Y. F. Geng, X. J. Li, and X. M. Hong, "High-sensitivity and large-range fiber optic temperature sensor based on pdms-coated mach-zehnder interferometer combined with fbg," Opt. Express **29**(12), 18624–18633 (2021).
16. X. Zeng, "Laser-induced fiber polymer axicon fabrication and application for spot scanning imaging on both reflection and transmission," Fibers Polym. **15**(11), 2416–2422 (2014).
17. J. Tan, R. Yu, and L. Xiao, "Bessel-like beams generated via fiber-based polymer microtips," Opt. Lett. **44**(4), 1007–1010 (2019).
18. A. Zhou, Y. Zhang, Q. Xu, J. Yang, and L. Yuan, "Semi-open cavity in-fiber mach-zehnder interferometer for temperature measurement with ultra-high sensitivity," Appl. Opt. **53**(12), 2696 (2014).
19. X. Fan, Q. Wang, M. Zhou, F. Liu, H. Shen, Z. Wei, F. Wang, C. Tan, and H. Meng, "Humidity sensor based on a graphene oxide-coated few-mode fiber mach-zehnder interferometer," Opt. Express **28**(17), 24682–24692 (2020).
20. Z. H. Wang, S. C. Jiang, P. Yang, W. X. Wei, W. G. Bao, and B. J. Peng, "High-sensitivity and high extinction ratio fiber strain sensor with temperature insensitivity by cascaded mzi and fpi," Opt. Express **31**(5), 7073–7089 (2023).
21. P. Gustafik, O. Sugihara, and N. Okamoto, "Optical properties of acrylate-based negative-type photoresist and its application to optical waveguide fabrication," Jpn. J. Appl. Phys. **43**(4S), 2011 (2004).
22. R. Bachelot, A. Fares, R. Fikri, D. Barchiesi, G. Lerondel, and P. Royer, "Coupling semiconductor lasers into single-mode optical fibers by use of tips grown by photopolymerization," Opt. Lett. **29**(17), 1971–1973 (2004).
23. L. M. Xiao, W. Jin, and M. S. Demokan, "Photopolymer microtips for efficient light coupling between single-mode fibers and small-core photonic crystal fibers," Photonic Appl. for Aerospace, Transp. Harsh Environ. **6379**, 637902 (2006).
24. L. V. Nguyen, D. Hwang, S. Moon, D. S. Moon, and Y. J. Chung, "High temperature fiber sensor with high sensitivity based on core diameter mismatch," Opt. Express **16**(15), 11369–11375 (2008).
25. B. Yin, Y. Li, Z. B. Liu, S. C. Feng, Y. L. Bai, Y. Xu, and S. S. Jian, "Investigation on a compact in-line multimode-single-mode-multimode fiber structure," Opt. Laser Technol. **80**, 16–21 (2016).
26. H. Y. Choi, M. J. Kim, and B. H. Lee, "All-fiber mach-zehnder type interferometers formed in photonic crystal fiber," Opt. Express **15**(9), 5711–5720 (2007).
27. K. Dey and S. Roy, "Analyzing spectral properties and sensing performance of multi-single-multi mode fiber combination," Phys. Scr. **97**(12), 125507 (2022).
28. R. Xiong, H. Y. Meng, Q. Q. Yao, B. Huang, Y. M. Liu, H. C. Xue, C. H. Tan, and X. G. Huang, "Simultaneous measurement of refractive index and temperature based on modal interference," IEEE Sens. J. **14**(8), 2524–2528 (2014).
29. Y. F. Chen, Y. Wang, R. Y. Chen, W. K. Yang, H. Liu, T. G. Liu, and Q. Han, "A hybrid multimode interference structure-based refractive index and temperature fiber sensor," IEEE Sens. J. **16**(2), 331–335 (2016).
30. L. Zhao, S. Hao, Y. H. Chen, E. M. Zhao, C. A. X. Xing, J. Fan, and J. N. Tang, "Simultaneous measurement of strain and temperature based on fiber sensor with vernier effect," Opt. Laser Technol. **157**, 108670 (2023).
31. C. Y. He, J. B. Fang, Y. A. Zhang, Y. Yang, J. H. Yu, J. Zhang, H. Y. Guan, W. T. Qiu, P. J. Wu, J. L. Dong, H. H. Lu, J. Y. Tang, W. G. Zhu, N. Arsad, Y. Xiao, and Z. Chen, "High performance all-fiber temperature sensor based on coreless side-polished fiber wrapped with polydimethylsiloxane," Opt. Express **26**(8), 9686–9699 (2018).
32. Q. Wang, C. Du, J. M. Zhang, R. Q. Lv, and Y. Zhao, "Sensitivity-enhanced temperature sensor based on pdms-coated long period fiber grating," Opt. Commun. **377**, 89–93 (2016).